ORIGINAL PAPER

Fusheng Tan · Qihong Fang · Jia Li · Hong Wu

Interaction of precipitate with shear–coupled grain boundary migration

Abstract Shear-coupled grain boundary migration (SCGBM) has already been observed in extensive experiments and serves as an effective mechanism for the grain growth in nanocrystalline materials. Meanwhile, it is well known that precipitates strongly inhibit the motion of GBs. However, the effect of precipitates on SCGBM is not clear. In this paper, a theoretical model is established to investigate the role of precipitates on SCGBM. The effects of the characteristics of the precipitate and the GB are studied in detail. It is found that precipitates can significantly inhibit SCGBM. Interesting, the results show that the pinning effect exerted by precipitates on SCGBM is strongly relevant to their positions. Moreover, the resistance for SCGBM hindered by precipitates can be controlled by tailoring the characteristics of both the precipitates and GBs. In addition, it is discussed that a possible recrystallization occurs when the GB is hindered and it is found that the SCGBM process also facilitates it.

1 Introduction

Nanocrystalline materials (NCMs) with nanoscale grains usually exhibit technologically interesting properties such as high strength, ductility and irradiation resistance [1–8]. For example, most metallic NCMs have ultra-high strength and hardness compared with their coarse-grained counterpart, because dislocations are extremely confined by their high-density GBs [2,4–7]; besides, experiments have demonstrated the possibility of attaining high-radiation-tolerant materials by minimizing grain sizes in the nanocrystalline regime [1]. In traditional coarse-grained materials, mechanical properties, such as strength and ductility, are controlled by dislocations. However, because the motion of the dislocation is extremely restricted in NCM, GB-assisted and GB-mediated deformation modes, including GB slip, migration and grain rotation, become the domination [2,3,9–14]. These modes always lead to grain coarsening which is unfavorable in most NCMs since it would weaken and soften the material [2]. Recently, stress-driven nanograin growth (NGG) has become of interest since it plays a significant role in the microstructures and properties of NCM [9–23].

Among these GB modes, the GBM is of particular interest that serves as a generic mode of NG and is also found to be related to the combination of high strength, ductility and toughness in NCM [5,9–14,22]. For instance, the migration of twin boundary is found to contribute to the combination of high strength and ductility of nanotwinned Cu [24–26]. Moreover, many GBs have the property that their normal migration is accompanied by a simultaneous relative translation of adjacent grains parallel to the GB plane [13,14,16,22,23]. Such GBs

F. Tan · Q. Fang · J. Li (✉)
State Key Laboratory of Advanced Design and Manufacturing for Vehicle Body, Hunan University,
Changsha 410082, People's Republic of China
E-mail: lijia123@hnu.edu.cn

H. Wu
State Key Laboratory of Powder Metallurgy, Central South University, Changsha 410083, People's Republic of China

are said to be coupled, since the GBM will occur if a shear stress is applied parallel to them, as revealed by extensive experiments and MD simulations. Moreover, theoretical studies have revealed that the SCGBM is more energetically favorable than the pure GBM, that is, without coupling effect [22].

It is common knowledge that precipitates play a key role in controlling the evolution of metal microstructures and their stability in precipitate-strengthening materials, owing to their strong pinning effect on the motion of dislocations and GBs [27–42]. The pinning force exerted by precipitates on GBM was first theoretically illustrated by the Zener model [32,36]. When validating by extensive studies, the Zener model can well describe the precipitates pinning effect on GBM in traditional materials with coarse grains [27,29,31,32,34,36,42]. Since the SCGBM is a special plastic mode in NCM, the pinning effect by precipitates on the SCGBM will be different, compared to its counterpart in traditional materials. However, the quantitative correlation remains unclear. The lack of accurate description of the precipitate pinning effect on the SCGBM limits the in-depth understanding of microstructural evolution and properties of NCM. Thereby, in this study, we theoretically investigate the SCGBM hindered by precipitates in NCM. Equilibrium energy characteristics of the process are calculated as those depending on the structural and geometric parameters of both GBs and precipitates. The effects of the size and position of precipitates, and the misorientation angle of GBs as well as the coupling factor of the SCGBM process, are studied in detail. Besides, a possible mechanism of recrystallization occurs when the SCGBM is hindered by precipitates, which is discussed at the end of this paper.

2 Geometry of SCGBM hindered by precipitates

The geometry of the SCGBM hindered by a precipitate is shown schematically in Fig. 1. An elastically isotropic two-dimensional nanograined microstructure with grains G1 and G2 divided by a GB AB is under consideration, as shown in Fig. 1a. Besides, a precipitate is located in grain G2. In our model, the GB AB can be modeled as a dislocation wall with identical Burgers vector b shown in Fig. 1a'. The case of the SCGBM hindered by a precipitate shown in Fig. 1d can be combined by the following two cases: (1) the general SCGBM that is not hindered by precipitates, as shown in Fig. 1b; (2) the pure GBM hindered by a precipitate, as shown in Fig. 1c.

Case (1) can be depicted in detail as follows: Under certain shear stress τ, the GB AB migrates in the normal direction by a distance m, which is simultaneously accompanied by a tangential translation s. The SCGBM process is characterized by a coupling factor $\beta = s/m$, and the value depending on the GB structure can reach 1 in experiments and MD simulations and 5 according to theoretical studies. The process ends up with the GB AB moving from its initial position to a new position CD, accompanied with a disclination quadrupole $ABCD$ with strength $\pm\omega_1$ generated at GB junctions. Here, the value of ω_1 is equal to the misorientation angle θ_0 of GB AB, and it ranges from $0°$ to $90°$ thus to cover both low-angle and high-angle GBs. The equivalent configuration of Fig. 1b is shown schematically in Fig. 1b'.

Case (2) is described in detail as follows: Under certain shear stress τ, the GB AB migrates forward in the normal direction by some distance and then interacts with a preexisting precipitate. According to extensive studies [29,31,32,36], the GB is flexible and thus it bends during the interaction. In detail, the GB AB can be divided into several segments, i.e., BH', $H'F'$, $F'E'$, $E'G'$ and $G'A$, according to its final states shown in Fig. 1c. These segments are discussed separately: ① The GB segments BH' and $G'A$ migrate by distance m to their new position DH and GC with unchanged GB structure, respectively. ② In general, GBM in a metal occurs through atomic rearrangements and the GB and in its vicinities in adjacent grain interiors. Such rearrangements are suppressed by the immobile precipitate. Thereby, the segment $F'E'$ migrates by distance $m - m_p$ to the new position FE and then it is stopped by the preexisting precipitate. ③ As mentioned above, when a migrating GB is hindered by precipitates, the part of the GB near the precipitate will bend. Besides, the precipitate pinning force will be maximized when the migrating GB bends to a certain level [29,32,35,36]. The accurate GB geometry in real materials is too complicated to fit perfectly in theory. To take the phenomenon into account, in our model, we assume that the GB segments $H'F'$ and $E'G'$ migrate and transform into the slant GB segments HF and EG, respectively. The two slant segments are both characterized by the geometric parameters m_p and s_p, as shown in Fig. 1c. Here, it is worth to note that the slant segments just serve as a first estimate of the bended GB in real materials, since the overall process of the transformation is complicated and its details are beyond the scale of the study. According to experiments [43,44], the precipitates pinning will not change the original shape of the GB a lot. In other words, for the plane GB examined in this paper, the directions of the slant segments HF and EG are basically the same as those of the others. That indicates that the dislocations in HF and EG can be approximately equivalent to the dislocations in the inset of Fig. 1c'. In this context, the dislocations in HF and EG can be represented by disclination dipoles shown in Fig. 1c.
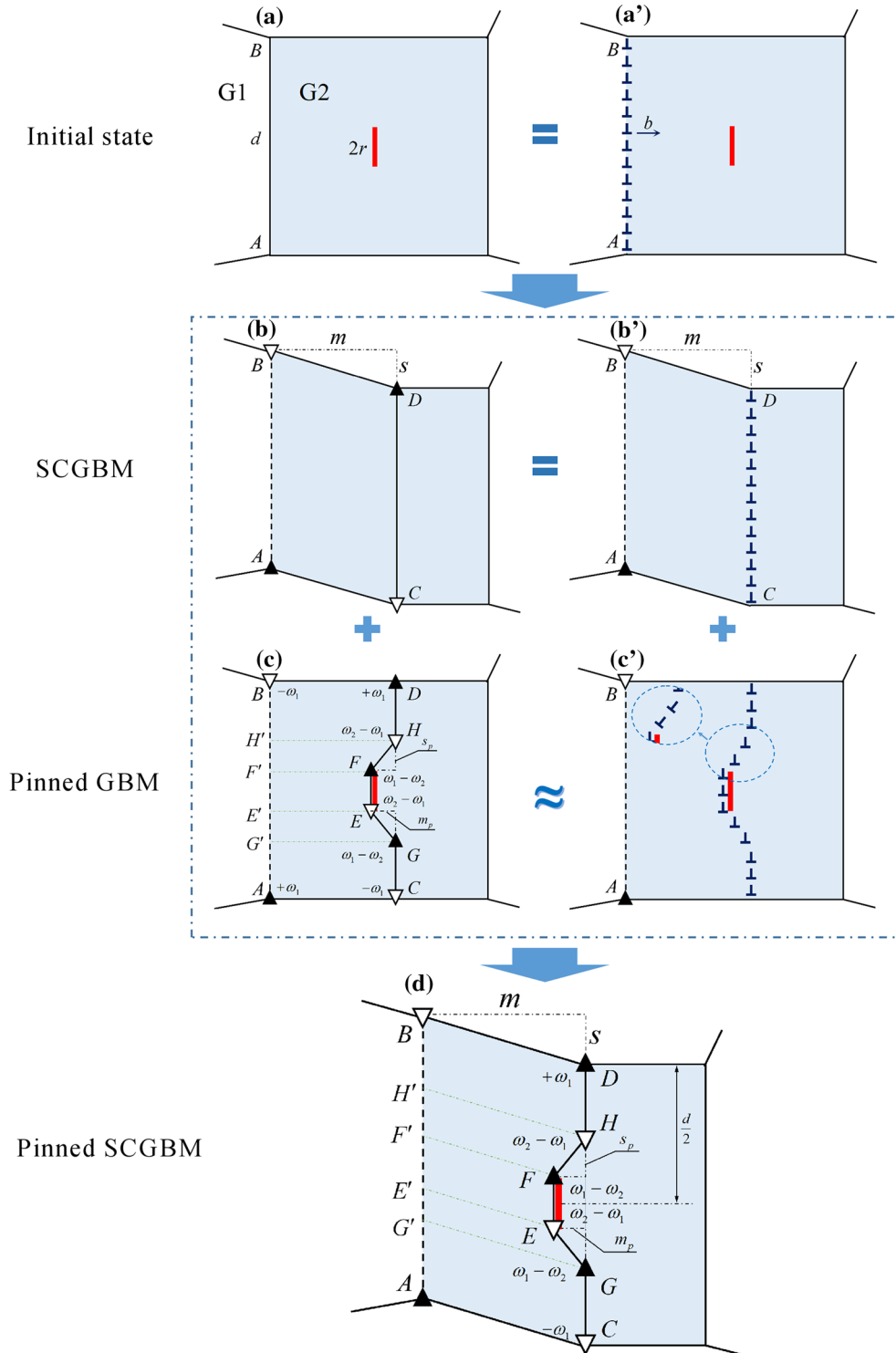
Fig. 1 Schematic diagrams of a general SCGBM and the pure GBM hindered by a precipitate. **a** Initial configuration of two grains, i.e., G1 and G2, divided by the GB *AB*. A precipitate (red elongated rectangle) is located in G2, **b** the general SCGBM is driven by shear stress, **c** the pure GBM is driven by the shear stress and then hindered by the precipitate, and **a'**, **b'** and **c'** are equivalent configurations of **a**, **b** and **c**, respectively, where the considered GBs are modeled as dislocation walls. The inset in (**c'**) represents the approximately equivalent configuration of the local GB dislocations circled by a dashed line. **d** The SCGBM is hindered by the precipitate. This process is equivalent to the combination of the general SCGBM (shown in **b**) and the pure GBM hindered by a precipitate (shown in **c**)

The values of m_p and s_p are accordingly set as $0.1r$ and $1.0r$, respectively. The setting takes into account the experimental fact that the area affected by the precipitate is of the same magnitude as the precipitate.

Combining cases (1) and (2), the SCGBM hindered by the precipitate can be obtained and is schematically shown in Fig. 1d. For simplicity, in our model, the precipitate is always assumed to locate at the same level of the center of the curved GB, which means $FD = EC$. In real materials, precipitates locate randomly on the GB and in the grain interior. However, since the study aims to address the main characteristics of the precipitate-hindered SCGBM, it is reasonable and enough to assume only one precipitate in the considered system and its position is set deliberately to simplify the following calculations. The precipitate is a few-layer nanoplatelet that has a characteristic length $2r$. The thickness of the precipitate is set at $0.1r$, and thus, it can be negligible in the calculation, since the results in the paper are not sensitive to the thickness.

As explained in case (2), the structures of the GB segments HF and EG are different from others. The difference essentially originates from the change in the density of dislocations in segments HF and EG, compared with their origin segments $H'F'$ and $E'G'$, respectively. To illustrate the difference a bit clearer, we consider the case of low-angle symmetrical tilt GB with length l_0 that is composed of n_0 aligned discrete dislocations. If the GB length changes from l_0 to l_t without changing the dislocation number, its misorientation angle will change from $\theta_0 = n_0 b/l_0$ to $\theta_t = n_0 b/l_t = (l_0/l_t) \theta_0$. The reduction in misorientation leads to a disclination dipole with strength $\pm \omega_t = \pm \theta_t$. In the considered model, it means a disclination quadrupole $EFHG$ with strength $\pm \omega_2 = \pm \left(s_p/\sqrt{s_p^2 + m_p^2} \right) \omega_1$ is generated because the GB interacts with the precipitate. As discussed in case 1), dislocation walls DH, FE and GC can be represented as disclination dipoles with strength $\pm \omega_1$, as shown in c. Therefore, by superimposing, the strength of the disclination quadrupole $EFHG$ is equal to $\pm (\omega_1 - \omega_2)$, as shown in Fig. 1.

3 Energy characteristics of the pure SCGBM

In this part, the energy changes ΔW_1 and ΔW_2 for the case of the general SCGBM and the SCGBM hindered by a precipitate will be calculated as those depending on the structural and geometric parameters, respectively. The detailed geometries of the SCGBM without and with precipitates are shown in Fig. 1b and d, respectively.

First, we would like to consider the general SCGBM process shown in Fig. 1b. Following previous studies [9–11,22,45], the energy change ΔW_1 can be calculated as:

$$\Delta W_1 = E_{AB} + E_{CD} + E_{AB}^{CD} - A_1, \tag{1}$$

where E_{AB} and E_{CD} are the energies of the disclination dipoles AB and CD, respectively. E_{AB}^{CD} is the energy term resulting from the interaction between the disclination dipoles AB and CD. A_1 is the work done by the applied shear stress τ for migrating the GB AB by distance m to its new position CD.

In a NCM with shear modulus G and Poisson ratio ν, the proper self-energy of the disclination dipoles AB and CD with strength $\pm \omega_1$ and arm d can be expressed as [9,15,22,46]:

$$E_{AB} = E_{CD} = \frac{D\omega_1^2 d^2}{2} \left[\ln \frac{R}{d} + \frac{1}{2} \right], \tag{2}$$

where $D = G/2\pi (1 - \nu)$ and R is the screening length of stress fields of the disclination dipoles. The interaction energy E_{AB}^{CD} can be calculated in a standard method as the work done in generating the disclination dipole CD in the stress field created by dipole AB [9–11,15,22,46]. Then, the energy term is expressed as follows:

$$E_{AB}^{CD} = \frac{D\omega_1^2}{2} \left[l_{AC}^2 \ln \frac{R}{l_{AC}} + l_{BD}^2 \ln \frac{R}{l_{BD}} - l_{AD}^2 \ln \frac{R}{l_{AD}} - l_{BC}^2 \ln \frac{R}{l_{BC}} + l_{AB} l_{CD} \right], \tag{3}$$

where the values of l_{AB}, l_{CD}, l_{AD} and l_{BC} are lengths of AB, CD, AD and BC, respectively. Their values are calculated based on the geometry shown in Fig. 1d and expressed as follows: $l_{AB} = l_{CD} = d, l_{AC} = l_{BD} = m\sqrt{1 + \beta^2}$, $l_{AD} = \sqrt{(d - \beta m)^2 + m^2}$ and $l_{BC} = \sqrt{(d + \beta m)^2 + m^2}$. By summing the proper self-energy E_{AB}, E_{CD} and the interaction energy E_{AB}^{CD}, the proper energy W_n^{pre} of the considered defect configuration $ABCD$ can be finally obtained, i.e., $W_n^{\text{pre}} = E_{AB} + E_{CD} + E_{AB}^{CD}$.

Following general approach, the work done by the shear stress τ in the general SCGBM process can be calculated as follows [22]:

$$A_1 = \tau \, dm \, (\omega + \beta).$$ (4)

Thus, based on Eqs. (2)–(4), the energy change ΔW_1 can be finally obtained. The calculation will serve as a comparison for the SCGBM hindered by the precipitate.

4 Energy characteristics of the SCGBM hindered by a precipitate

For the case of SCGBM hindered by a precipitate, a disclination quadrupole $EFHG$ with strength $\pm (\omega_1 - \omega_2)$ is generated, as shown in Fig. 1d. The energy change ΔW_2 in the considered case includes two parts:

$$\Delta W_2 = W_y^{\text{pre}} - A_2,$$ (5)

where the first and second terms represent the total energy of the defect configuration and the word done by the stress τ in moving the initial GB AB to the new GB (combined with segments DH, HF, FE, EG and GC), respectively.

The energy term W_y^{pre} includes the self-energies of the disclination dipoles and their interaction energies:

$$W_y^{\text{pre}} = E_{AB} + E_{EF} + E_{GH} + E_{CD} + E_{AB}^{EF} + E_{AB}^{GH} + E_{AB}^{CD} + E_{EF}^{GH} + E_{EF}^{CD} + E_{GH}^{CD} + E_{\text{surf}},$$ (6)

where the energy terms E_{AB}, E_{EF}, E_{GH} and E_{CD} are the self-energies of the disclination dipoles AB, EF, GH and CD, respectively. The energy terms E_{AB}^{EF}, E_{AB}^{GH}, E_{AB}^{CD}, E_{EF}^{GH}, E_{EF}^{CD} and E_{GH}^{CD} specify the interaction energies between AB–EF, AB–GH, AB–CD, EF–GH, EF–CD and GH–CD, respectively. The last term represents the increment in the GB surface energy because the total area of migrating GB increases, resulting from the presence of slant segments HF and EG.

Follows general approach, for a disclination dipole with strength $\pm \omega_i$ and arm p_i, the proper self-energy can be calculated as [9,10,15,22,46,47]:

$$W^{\text{self}}(\omega_i, \, p_i) = \frac{D \omega_i^2 p_i^2}{2} \left(\ln \frac{R}{p_i} + \frac{1}{2} \right).$$ (7)

Therefore, the self-energies in Eq. (6) can be expressed as follows:

$$\begin{aligned}
E_{AB} &= E_{CD} = W^{\text{self}}(\omega_1, \, d), \\
E_{EF} &= W^{\text{self}}(\omega_1 - \omega_2, \, 2r), \\
E_{GH} &= W^{\text{self}}(\omega_1 - \omega_2, \, 2r + 2s_p).
\end{aligned}$$ (8)

By adopting the standard method that treats the interaction energy E_i^j as the work done for generating the disclination dipole j in the stress field created by the disclination dipole i, the interaction energies in Eq. (6) are written as:

$$\begin{aligned}
E_{AB}^{EF} &= W^{\text{int}}(\omega_1, \omega_1 - \omega_2, l_{AB}, l_{EF}, l_{AF}, l_{BE}, l_{AE}, l_{BF}), \\
E_{AB}^{GH} &= W^{\text{int}}(\omega_1, \omega_2 - \omega_1, l_{AB}, l_{GH}, l_{AH}, l_{BG}, l_{AG}, l_{BH}), \\
E_{AB}^{CD} &= W^{\text{int}}(\omega_1, \omega_1, l_{AB}, l_{CD}, l_{AD}, l_{BC}, l_{AC}, l_{BD}), \\
E_{EF}^{GH} &= W^{\text{int}}(\omega_1 - \omega_2, \omega_1 - \omega_2, l_{EF}, l_{GH}, l_{EH}, l_{FG}, l_{EG}, l_{HF}), \\
E_{EF}^{CD} &= W^{\text{int}}(\omega_1 - \omega_2, \omega_1, l_{EF}, l_{CD}, l_{ED}, l_{FC}, l_{EC}, l_{DF}), \\
E_{GH}^{CD} &= W^{\text{int}}(\omega_1 - \omega_2, \omega_1, l_{GH}, l_{CD}, l_{GD}, l_{HC}, l_{GC}, l_{DH}),
\end{aligned}$$ (9)

where the general formula of the interaction energy W^{int} is expressed as [9,10,15,18,46,47]:

$$\begin{aligned}
&W^{\text{int}}(\omega_i, \omega_j, p_i, p_j, l_i, l_j, q_i, q_j) \\
&= \frac{D \omega_i \omega_j}{2} \left(q_i^2 \ln \frac{R}{q_i} + q_j^2 \ln \frac{R}{q_j} - l_i^2 \ln \frac{R}{l_i} - l_j^2 \ln \frac{R}{l_j} - p_i p_j \right).
\end{aligned}$$ (10)

The parameters in Eq. (9) can be calculated based on the geometry shown schematically in Fig. 1d. Their expressions are given as follows:

$$l_{EF} = 2r, \; l_{GH} = 2\left(r + s_p\right), \; l_{FH} = l_{EG} = \sqrt{m_p^2 + s_p^2}, l_{AC} = l_{BD} = \sqrt{m^2\left(1 + \beta^2\right)},$$

$$l_{AE} = \sqrt{\left(m - m_p\right)^2 + \left(\tfrac{d}{2} - r - s\right)^2}, l_{AF} = \sqrt{\left(m - m_p\right)^2 + \left(\tfrac{d}{2} + r - s\right)^2},$$

$$l_{BE} = \sqrt{\left(m - m_p\right)^2 + \left(\tfrac{d}{2} + r + s\right)^2}, l_{BF} = \sqrt{\left(m - m_p\right)^2 + \left(\tfrac{d}{2} - r + s\right)^2},$$

$$l_{AG} = \sqrt{m^2 + \left(\tfrac{d}{2} - r - s\right)^2}, l_{AH} = \sqrt{m^2 + \left(\tfrac{d}{2} + r + s_p - s\right)^2}, \quad (11)$$

$$l_{BH} = \sqrt{m^2 + \left(\tfrac{d}{2} - r - s_p + s\right)^2}, l_{BG} = \sqrt{m^2 + \left(\tfrac{d}{2} + r + s_p + s\right)^2},$$

$$l_{EH} = l_{FG} = \sqrt{m_p^2 + \left(2r + s_p\right)^2}, l_{DH} = l_{GC} = \tfrac{d}{2} - r - s_p, l_{GD} = l_{CH} = \tfrac{d}{2} + r + s_p.$$

The term E_{surf} is calculated as follows:

$$E_{\text{surf}} = 2\gamma_{\text{surf}}\left(\sqrt{m_p^2 + s_p^2} - s_p\right), \quad (12)$$

where the term γ_{surf} is the density of GB surface energy. Substituting Eqs. (7)–(12) into Eq. (6), the energy W_y^{pre} that specifies the proper energy of the considered defect configuration is finally obtained.

The work A_2 is expressed as follows [10,22,46]:

$$A_2 = \tau\left(\omega_1 + \beta\right)\left[\left(d - 2r - 2s_p\right)m + 2r\left(m - m_p\right) + 2cs_p\left(m - m_p/2\right)\right], \quad (13)$$

where the first term characterizes the work done for moving the segments BH' and GA', the second for moving the segment $F'E'$ and the third for moving the segments $H'F'$ and $E'G'$. Here, it is worth to note that the third term is an estimated value, since the precise one is hard to be obtained. As mentioned before, the segments HF and EG result from the transformation of segments $H'F'$ and $E'G'$, respectively. That is why the third term in Eq. (12) cannot be computed in the same way as the first two terms. Here, it is first assumed that the segments $H'F'$ and $E'G'$ migrate by distance $m - m_p/2$ and then are multiplied by a coefficient c to manage the estimation. The value of c is smaller than 1, since the two GB segments have not yet moved to the same plane as CD—the final position of the migrating GB. The value of c is taken as 1/2, assuming that the dislocations in the slant segments distribute evenly.

Finally, based on Eqs. (5)–(13), one can finally investigate the SCGBM process hindered by a precipitate. Now the energy change ΔW_1 and ΔW_2 can be calculated based on Eqs. (1)–(4) and (5)–(13), respectively. The two processes are energetically favorable if $\Delta W_i < 0$. In the study of precipitate pinning GBM, another interest is the pinning effect exerted by the precipitate on the considered GB. In the model, the pinning force is defined as the difference between the two energy changes ΔW_1 and ΔW_2, i.e., $W_{\text{pin}} = \Delta W_2 - \Delta W_1$. Here, it is worth to emphasize that the pinning force is only a part of the resistance of the SCGBM process, and it mainly derives from the interaction between the disclination quadrupole $EFHG$ and the other disclinations. Another part of the resistance originates from the general SCGBM process, which derives from the attraction of the disclination dipoles AB and CD. These energies are calculated in the exemplary case of Cu matrix specified by the shear modulus $G = 44$ GPa and Poisson ratio $\nu = 0.3$. The density of GB surface energy is taken as $\gamma_{\text{surf}} = 0.5$ J/m^2.

5 Results and discussion

Figure 2 shows the typical dependencies of the energy changes ΔW_1 and ΔW_2 on the GB migration distance m, for different shear stresses τ (Fig. 2a) and precipitate sizes $2r$ (Fig. 2b). Other parameters are taken as $\beta = 1$, $\omega_1 = 0.2$ and $d = 100$ nm. It is found that the SCGBM is more difficult in the presence of the precipitate ($r = 0.15d$) than in the absence of precipitate ($r = 0$), which means that the precipitate indeed serves as a strong obstacle for the SCGBM. As shown in Fig. 2a, under small stress, i.e., $\tau < 0.2D\omega_1$, the SCGBM is totally inhibited by the precipitate. Besides, for $\tau < 0.2D\omega_1$, the resistance increases monotonously with the increase in the migration distance. From Fig. 2a, one can also find that the difference W_{pin} between the two cases of SCGBM increases along with the increase in the migration distance. That indicates that the pinning
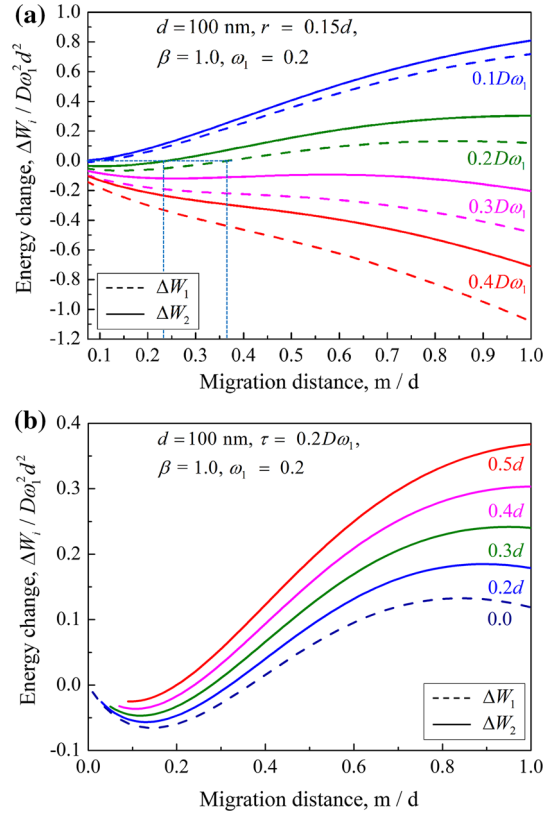
Fig. 2 Dependences of the energy change ΔW_1 (dash lines) and ΔW_2 (solid lines) of a 100-nm grained NCM Cu specimen with the migration distance m, for different normalized shear stresses $\tau/D\omega_1$ (**a**) and normalized precipitate sizes $2r/d$ (**b**). The dark blue dotted lines in (**a**) indicate the critical position of the migrating GB (color figure online)

effect will be stronger when the GB migrates by a long distance, which is also shown in Fig. 2b. This result is interesting, because it suggests that the effect of precipitates on SCGBM is highly relevant to the initial position of the migrating GB.

Here, it is necessary to note that if the SCGBM is hindered, the precipitate is always set to locate behind the migrating GB by distance m_p. Schematically speaking, in the case that the precipitate exists, the migrating GB drags the precipitate and moves. That is the main characteristic and also the limitation of the model, which can be found from the geometry of the model. Therefore, the dependence $\Delta W_2(m)$ in fact reflects the resistance at the GB when its migration distance reaches m, or the precipitate locates at $m - m_p$.

In traditional coarse-grained materials, the pinning force exerted by precipitates is not related to the distance between the precipitates and the initial GB position, as described in the Zener model and other models [29,31, 32,34–36,48]. Besides, the pinning force in these models originates from the GB tension, which is not related to the initial position of migrating GB. However, in the process of the SCGBM hindered by precipitates, the pinning force derives from the interaction of disclinations, some of which are located at the junctions of the initial GB *AB*. The nanoscale grains in NCM lay the ground for the interaction between disclinations, whose interactions are weak in coarse-grained materials due to the long distances between them. Therefore, the pinning force increases along with the increase in the migration distance. The general SCGBM shares the similar circumstance. Moreover, the SCGBM hindered by precipitates encounters with larger resistance due to the extra attraction between disclination dipoles *AB* and *EF*–*GH*, as shown in Fig. 1d.

Figure 2a shows that when the shear stress reaches a certain value ($\tau > 0.3D\omega_1$), no matter whether the precipitate exists or not, the SCGBM is energetically favorable at any migration distance m. Meanwhile, the resistance for SCGBM reduces at a larger migration distance. A critical case for the hindered SCGBM can be found at $\tau = 0.2D\omega_1$, at which the hindered SCGBM is energetically favorable when the migration distance $m < 0.24d$ and becomes unfavorable when the distance $m > 0.24d$. The results are in well consistent with previous studies [10,22]. A similar result is also shown in Fig. 2b, in which the hindered SCGBM is only energetically favorable at a small migration distance. Therefore, we may safely draw the conclusion that there
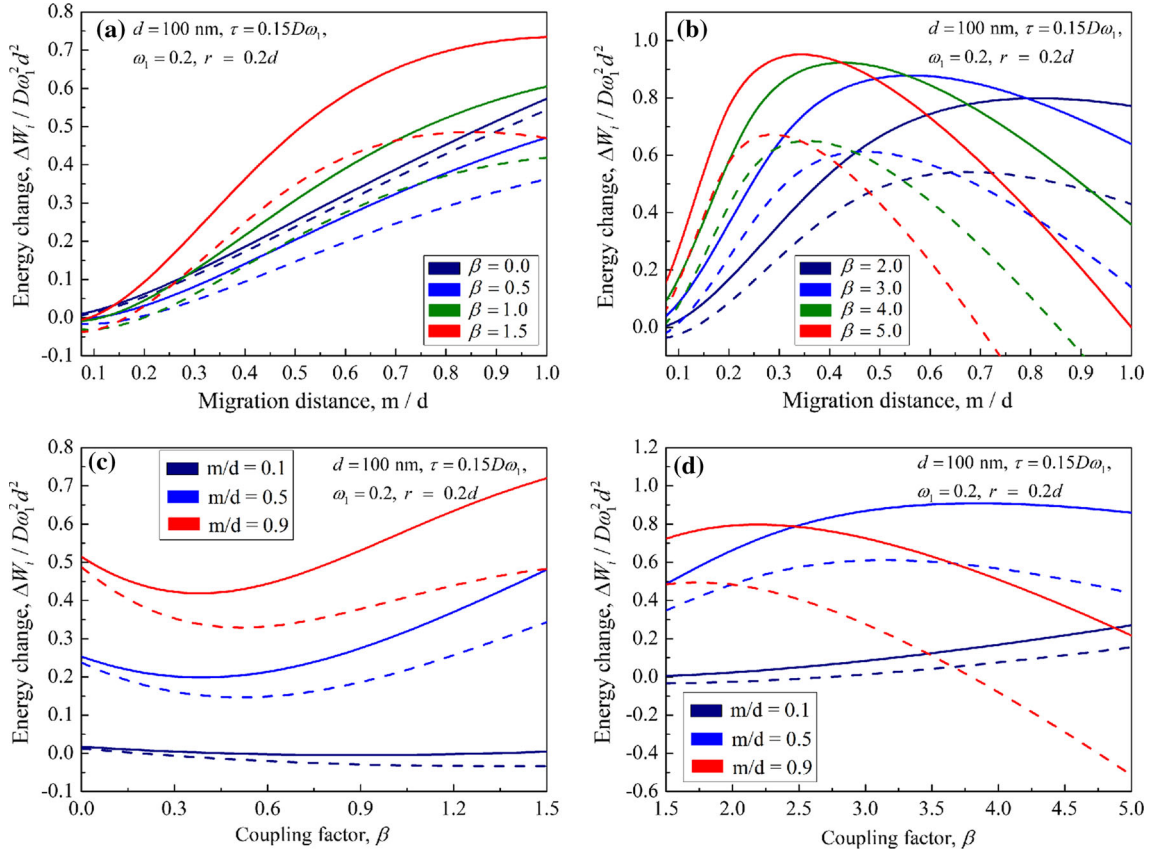
Fig. 3 Variation of the energy changes ΔW_1 (dash lines) and ΔW_2 (solid lines) with respect to the normalized migration distance m/d for different coupling factor levels is depicted in (**a**) and (**b**). **a** Depicts the cases of smaller coupling factors, i.e., $0 < \beta < 1.5$, while **b** depicts the cases of larger coupling factors, i.e., $1.5 < \beta < 5$. **c** and **d** are plots of the energy changes ΔW_1 (dash lines) and ΔW_2 (solid lines) on the coupling factor β for different migration distances m. Here, **c** depicts the case of $0 < \beta < 1.5$, while **d** the case of $1.5 < \beta < 5$

are certainly ranges for both applied stress τ and precipitate size $2r$, in which the hindered SCGBM can occur only in a small distance. The result suggests that the level of SCGBM can be controlled in some degree by tailoring the precipitate size properly.

The dependences of the energy changes ΔW_1 and ΔW_2 on the migration distance m, for different coupling factors β in the smaller and larger values, are depicted in Figs. 3a and b, respectively. The value of the coupling factor is determined by the structure of the considered GB, and it can reach 1 in experiments [12,13] and MD simulations [16,49] and 5 in theoretical studies [50,51]. Similarly, the hindered SCGBM is more difficult than the general SCGBM. Besides, the pinning effect is stronger when the GB is in the larger migration distance. When the coupling factor $\beta < 1.5$, both the resistance for SCGBM and the pinning force increase along with the increase in the migration distance, as shown in Fig. 3a. However, the resistance first increases and then decreases as the migration distance increases, when the coupling factor $\beta > 1.5$. Meanwhile, the gap between ΔW_1 and ΔW_2, i.e., W_{pin}, is larger at higher values of coupling factor. For example, for the case of $m = 1.0d$, the value of W_{pin} changes from around $0.025 D\omega_1^2 d^2$ to $0.3 D\omega_1^2 d^2$ as β varies from 0 to 1.5. That is, the pinning force increases with the increase in the coupling factor.

To investigate the effect of coupling factor β a bit clearly, the dependences of energy changes $\Delta W_1 (\beta)$ and $\Delta W_2 (\beta)$, for different migration distances m, are depicted in Figs. 3c and d, respectively. The dependences $\Delta W_i (\beta)$ in the range of $0 < \beta < 1.5$ are shown in Fig. 3c, in which a minimum value of the energy change is surprisingly found in $0.3 < \beta < 1.0$, in the case of hindered SCGBM. Considering that the observed coupling factor is not higher than 1 in experiments [12,13], the result suggests that the NG in NCM containing precipitates can be strongly inhibited in the experiment by reducing the coupling factor below 0.3, or promoting it above 1.0. Moreover, it is found that the minimization of energy change is not that significant at small value
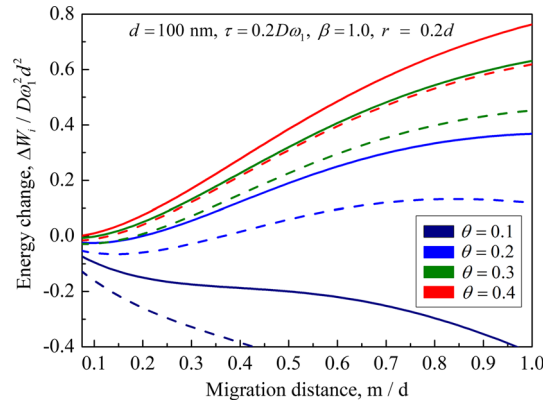
Fig. 4 Plots of the energy changes ΔW_1 (dash lines) and ΔW_2 (solid lines) versus the normalized migration distance m/d for a NC Cu of 100 nm grain size with various misorientation angles, i.e., $\theta = 0.1, 0.2, 0.3$ and 0.4

of m. That indicates that the minimization of resistance by tailoring the coupling factor is meaningless when the precipitate is close to the initial GB. The result is also shown in Fig. 3d.

According to Fig. 3d, similarly, the minimization of resistance by tailoring the coupling factor is meaningless when the precipitate is close to the initial GB. However, if the precipitate is far away from the initial GB (i.e., the precipitate is initially located inside the nanograin), further increasing the coupling factor may result in a sharp reduction in the resistance. For example, at $m/d = 0.9$, the resistance reduces sharply when the value of β is larger than 2.5.

From what has been discussed above, it is notable that the effect of the coupling factor on the hindered SCGBM is complicated. Increasing the coupling factor always leads to an increase in the pinning force, as discussed above, but it may not meet the goal that inhibits SCGBM. For example, in Fig. 3c, the resistance maximizes at $\beta = 0$, but the pinning effect is the weakest, when the migration distance $m/d = 0.1$ or 0.9. More extreme cases are shown in Fig. 3d, in which the energy change $\Delta W_2\ (\beta)$ encounters with a sharp reduction when the value of β is larger than 2.5 and when the migration distance $m/d = 0.9$.

Taking all these factors into account, we may safely suggest that when most precipitates distribute near GBs, inhibiting the shear-coupling effect on GBM can effectively hinder NGG; but when most precipitates are in the nanograin interior, increasing the factor β above 0.5 can achieve the goal of stabilizing NGM better.

Figure 4 presents the variation of the energy change ΔW_1 and ΔW_2 with the migration distance m for various misorientation angles of the migrating GB. The figure shows that the energy change ΔW_2 increases monotonously when $\theta > 0.2$ and decreases monotonously at $\theta = 0.1$. A similar tendency is also found in the energy change ΔW_1, which means the hindered SCGBM and the general one share a similar sensibility on the GB misorientation. As mentioned above, the misorientation angle θ varies from 0 to $\pi/2$ thus to cover the low-angle and high-angle GBs. Thus, the results indicate that, even hindered by the precipitate, the SCM is still more likely to occur in terms of the low-angle GBs. Moreover, it is found that the SCM of the GB in a slightly larger misorientation will be strongly inhibited. For instance, the hindered SCGBM is totally energetically unfavorable when increasing the misorientation angle θ from 0.1 to 0.3, as shown in Fig. 4. Considering that the high-angle GBs are the domination in extensive NCM, the result means that the NGG in a precipitate-strengthening NCM encounters a strong resistance.

The effect of the misorientation on the pinning effect is also obtained in Fig. 4, by comparing the values of ΔW_1 and ΔW_2, i.e., the effect on the value of W_{pin}. Obviously, the pinning effect decreases with the increase in misorientation. For example, at $m/d = 1.0$, the value of W_{pin} decreases from $0.2D\omega_1^2 d^2$ to $0.1D\omega_1^2 d^2$ as the misorientation angle θ is increased from 0.2 to 0.4, which indicates that precipitates are likely to generate a large pinning force on low-angle GBs. However, considering that reducing the misorientation angle leads to a decrease in the whole resistance for the hindered SCGBM, it is reasonable to infer that the NCM is more stable when there are more high-angle GBs.

6 Recrystallization when SCGBM is hindered by precipitates

In this part, a possible mechanism of recrystallization when the SCGBM is hindered by precipitates is proposed, based on previous studies. Consider the configuration in Fig. 1d as an initial one, the possible geometry of
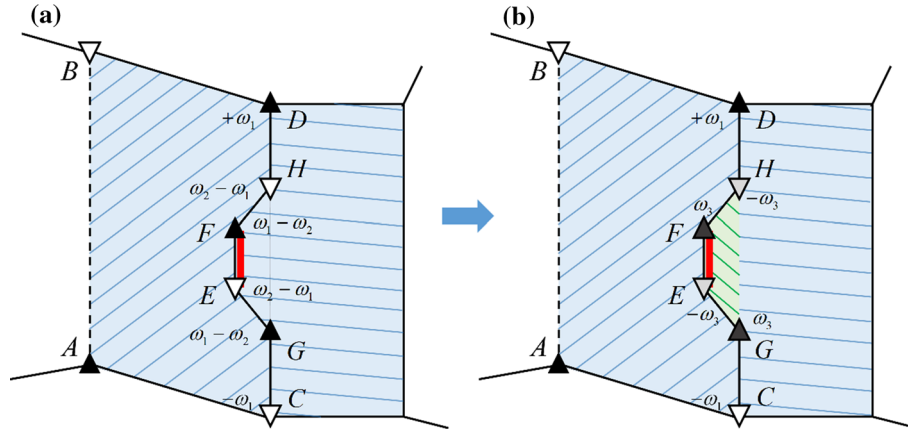
Fig. 5 Schematic diagram of the recrystallization when the SCGBM is hindered by the preexisting precipitate. **a** Initial configuration of the system, which is equivalent to Fig. 1d. **b** The recrystallization occurs along with the change in the strength of disclination quadrupole *EFHG*

the recrystallization is shown in Fig. 5. It is common knowledge that recrystallization results from the release of the local strain energy [52–56] and is commonly accompanied by GB bulging [53,57,58]. As shown in Fig. 5a, the migrating GB bends because it is hindered by a preexisting precipitate (see details in Fig. 1). The curved part of the GB is regarded as the result of GB protrusion and thus naturally becomes the nucleation point of recrystallization. The recrystallization consumes local strain energy, along with the change in the strength of the around disclinations, as shown in Fig. 5b. In other words, the disclinations release strain energy and activate recrystallization, thus weakening the disclinations. After the recrystallization, the strength of disclination quadrupoles *EFHG* changes from $\pm (\omega_1 - \omega_2)$ to $\pm \omega_3 = \pm e (\omega_1 - \omega_2)$. Here, the coefficient $e \,(> 0)$ represents the extent of this change. The recrystallization is characterized by the energy change $\Delta W_{re} = W_y^{\text{pre}} (\omega_3) - W_y^{\text{pre}} (\omega_1 - \omega_2)$. Here, the term $W_y^{\text{pre}} (\omega_1 - \omega_2)$ is calculated in the same approach as Eq. (6), and the term $W_y^{\text{pre}} (\omega_3)$ can be obtained by replacing the whole $(\omega_1 - \omega_2)$ with ω_3 in Eq. (6). The recrystallization is energetically favorable if $\Delta W_{re} < 0$.

Figure 6 shows the variation of the energy change ΔW_{re} with respect to the migration distance m of a 100-nm NC Cu sample. It is shown in Fig. 6a that the recrystallization is energetically favorable in most cases when the strength of the disclination quadrupole *EFHG* increases (i.e., $e > 1$) compared with its initial strength $\omega_1 - \omega_2$. It is reasonable since the recrystallization always leads to a gap of a misorientation angle between the nucleated grain and its adjacent grains [52,55–57]. Besides, the energy change ΔW_{re} decreases monotonously with the increase in the migration distance m, indicating that precipitates initially located inside the nanograin are more likely to induce the recrystallization after the SCGBM is hindered. The result is not sensitive to the precipitate size and coupling factor, as shown in Fig. 6b and c.

The result from Fig. 6b shows that increasing the precipitate size facilitates the recrystallization, which is in well consistent with previous literature [52–56,58]. It is already found in extensive experiments that the small second-phase particles effectively hinder GBM [27,31,32,42,58–61], while the big ones induce adjacent recrystallization [54–56,58]. Generally, in coarse-grained materials, large particles will produce a strong distortion stress field around them, which serves as an effective driving force for recrystallization. Thus, the result indicates another possible mechanism for the recrystallization in precipitate-strengthening NCM, which occurs when the SCGBM is hindered by precipitates.

The effect of the coupling factor β on the recrystallization is another interest, and it is shown in Fig. 6c. It is shown that the coupling factor effectively decreases the energy change ΔW_{re}, which indicates the coupling factor may turn the originally unfavorable ($\Delta W_{re} > 0$) recrystallization into favorable ($\Delta W_{re} < 0$). However, the maximum coupling factor observed in experiments is just 1, as mentioned above. Meanwhile, the results from Fig. 3c reveal that, in the range of $0 < \beta < 1$, the resistance for SCGBM maximizes at $\beta = 1$. Note that the SCGBM occurs first and the recrystallization is activated later and the fact that precipitate hindering leads to material hardening while the recrystallization leads to softening. Therefore, increasing the coupling factor of SCGBM can enhance the strength of NCM as well as the plasticity after the deformation.
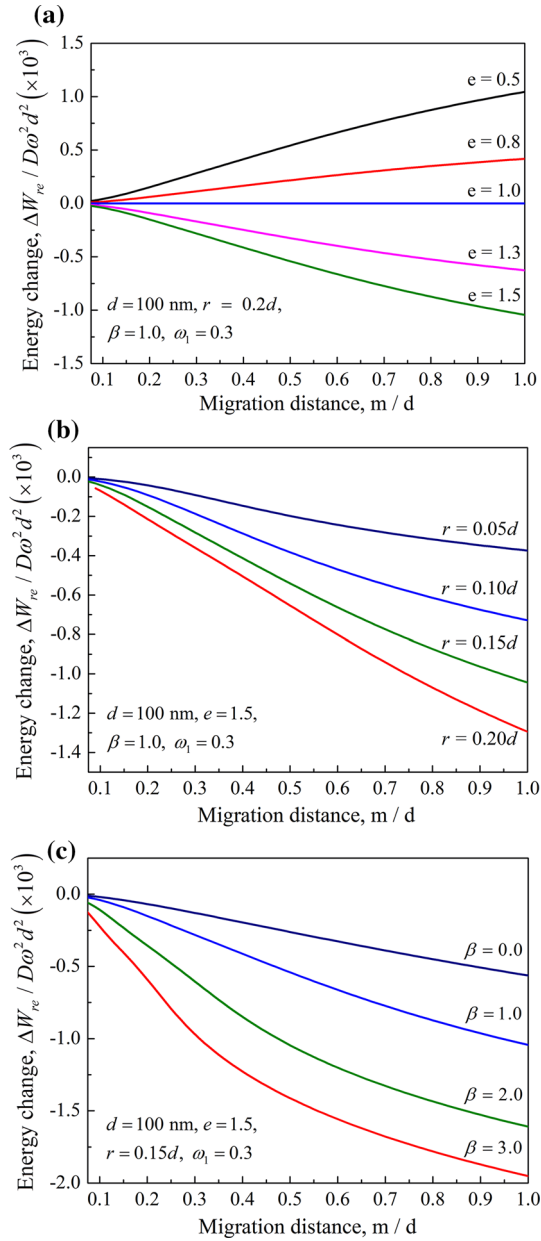
Fig. 6 Dependences of the energy change ΔW_{re} of a 100-nm grained NC Cu specimen with the normalized migration distance m/d, for various values of change level e (**a**), precipitate size $2r$ (**b**) and coupling factor β (**c**)

7 Conclusion

In this paper, a theoretical model is established to investigate the effect of precipitates on the SCGBM in NCM. Disclinations are generated during the SCGBM process and when the process is hindered by the precipitate, thus influencing the SCGBM process. The effects of the size and position of the precipitates, the misorientation angle of the GB and the coupling factor of the SCGBM process are studied in detail. The results obtained for a NC Cu sample show that precipitates serve as a significant obstacle for SCGBM and thereby enhance the stability of NC in precipitate-strengthening NCM. The high pinning force can be attributed to the larger precipitate size, migration distance of the GB, coupling factor that specifies the SCGBM process and the smaller misorientation angle of the migrating GB. Interesting, the total resistance of the SCGBM is not consistent with the trend of pinning force produced by the precipitate. The whole resistance of the SCGBM decreases when the

applied stress or the coupling factor increases to a certain level, which originates from the original characteristic of the general SCGBM process.

After that, a possible recrystallization in NCM is also discussed based on the model. The recrystallization occurs when the SCGBM is hindered by precipitates. It is found that the recrystallization is more likely to occur when GBs are hindered by the precipitates initially located in the nanograin interior. The effects of the precipitate size and coupling factor are investigated. The results show that increasing the precipitate size facilitates the recrystallization in NCM, which is similar to the case in coarse-grained materials. Moreover, it is found that the increase in the coupling factor is beneficial to the recrystallization.

In a word, the results obtained in the study suggest that precipitates effectively hinder the SCGBM process and thereby the NC in NCM. Besides, precipitates can also facilitate recrystallization and thus enhance the plastic deformation capacity of NCM. Both the above effects can be controlled by tailoring the characteristics of the precipitates and the GBs.

References

1. El-Atwani, O., Esquivel, E., Aydogan, E., Martinez, E., Baldwin, J.K., Li, M., Uberuaga, B.P., Maloy, S.A.: Unprecedented irradiation resistance of nanocrystalline tungsten with equiaxed nanocrystalline grains to dislocation loop accumulation. Acta Mater. **165**, 118–128 (2019)
2. Hu, J., Shi, Y.N.: Grain boundary stability governs hardening and softening in extremely-fine nanograined metals. Science **355**(2), 1292 (2017)
3. Li, Y., Zhang, Z., Vogt, R., Schoenung, J.M., Lavernia, E.J.: Boundaries and interfaces in ultrafine grain composites. Acta Mater. **59**(19), 7206–7218 (2011)
4. Barai, P., Weng, G.J.: Mechanics of very fine-grained nanocrystalline materials with contributions from grain interior, GB zone, and grain-boundary sliding. Int. J. Plast. **25**(12), 2410–2434 (2009)
5. Fan, G.J., Fu, L.F., Choo, H., Liaw, P.K., Browning, N.D.: Uniaxial tensile plastic deformation and grain growth of bulk nanocrystalline alloys. Acta Mater. **54**(18), 4781–4792 (2006)
6. Fang, T.H., Li, W.L., Tao, N.R., Lu, K.: Revealing extraordinary intrinsic tensile plasticity in gradient nano-grained copper. Science **331**(6024), 1587–1590 (2011)
7. Wu, X.L., Zhu, Y.T., Wei, Y.G., Wei, Q.: Strong strain hardening in nanocrystalline nickel. Phys. Rev. Lett. **103**(20), 205504 (2009)
8. Wei, Y., Li, Y., Zhu, L., Liu, Y., Lei, X., Wang, G., Wu, Y., Mi, Z., Liu, J., Wang, H.: Evading the strength-ductility trade-off dilemma in steel through gradient hierarchical nanotwins. Nat. Commun. **5**(4), 3580 (2014)
9. Bobylev, S.V., Ovid'Ko, I.A.: Stress-driven migration of deformation-distorted grain boundaries in nanomaterials. Acta Mater. **88**, 260–270 (2015)
10. Li, J., Soh, A.K.: Synergy of grain boundary sliding and shear-coupled migration process in nanocrystalline materials. Acta Mater. **61**(14), 5449–5457 (2013)
11. Gutkin, M.Y., Ovid'Ko, I.A.: Grain boundary migration as rotational deformation mode in nanocrystalline materials. Appl. Phys. Lett. **87**(25), 251916 (2005)
12. Gorkaya, T., Molodov, D.A., Gottstein, G.: Stress-driven migration of symmetrical 1 0 0 tilt grain boundaries in Al bicrystals. Acta Mater. **57**(18), 5396–5405 (2009)
13. Mompiou, F., Caillard, D., Legros, M.: Grain boundary shear–migration coupling—I. In situ TEM straining experiments in Al polycrystals. Acta Mater. **57**(7), 2198–2209 (2009)
14. Rajabzadeh, A., Legros, M., Combe, N., Mompiou, F., Molodov, D.A.: Evidence of grain boundary dislocation step motion associated to shear-coupled grain boundary migration. Philos. Mag. **93**(10–12), 1299–1316 (2013)
15. Bobylev, S.V., Ovid'ko, I.A.: Stress-driven migration, convergence and splitting transformations of grain boundaries in nanomaterials. Acta Mater. **124**, 333–342 (2017)
16. Cahn, J.W., Mishin, Y., Suzuki, A.: Coupling grain boundary motion to shear deformation. Acta Mater. **54**(19), 4953–4975 (2006)
17. He, M.-R., Samudrala, S.K., Kim, G., Felfer, P.J., Breen, A.J., Cairney, J.M., Gianola, D.S.: Linking stress-driven microstructural evolution in nanocrystalline aluminium with grain boundary doping of oxygen. Nat. Commun. **7**, 11225 (2016)
18. Ovid'ko, I.A., Sheinerman, A.G.: Free surface effects on stress-driven grain boundary sliding and migration processes in nanocrystalline materials. Acta Mater. **121**, 117–125 (2016)
19. Thomas, S.L., Chen, K., Han, J., Purohit, P.K., Srolovitz, D.J.: Reconciling grain growth and shear-coupled grain boundary migration. Nat. Commun. **8**(1), 1764 (2017)
20. Wang, X., Zeng, W., Hong, L., Xu, W., Yang, H., Wang, F., Duan, H., Tang, M., Jiang, H.: Stress-driven lithium dendrite growth mechanism and dendrite mitigation by electroplating on soft substrates. Nat. Energy **3**(3), 227 (2018)
21. Zhang, Y., Tucker, G.J., Trelewicz, J.R.: Stress-assisted grain growth in nanocrystalline metals: Grain boundary mediated mechanisms and stabilization through alloying. Acta Mater. **131**, 39–47 (2017)
22. Li, J., Soh, A.K.: On shear-coupled migration of grain boundaries in nanocrystalline materials. Appl. Phys. Lett. **101**(24), 241915 (2012)
23. Ivanov, V.A., Mishin, Y.: Dynamics of grain boundary motion coupled to shear deformation: an analytical model and its verification by molecular dynamics. Phys. Rev. B Condens. Matter **78**(6), 064106 (2008)

24. Li, X., Wei, Y., Lu, L., Lu, K., Gao, H.: Dislocation nucleation governed softening and maximum strength in nano-twinned metals. Nature **464**(7290), 877 (2010)
25. Lu, L., Chen, X., Huang, X., Lu, K.: Revealing the maximum strength in nanotwinned copper. Science **323**(5914), 607–610 (2009)
26. Shen, Y.F., Lu, L., Lu, Q.H., Jin, Z.H., Lu, K.: Tensile properties of copper with nano-scale twins. Scr. Mater. **52**(10), 989–994 (2005)
27. Koju, R.K., Darling, K.A., Solanki, K.N., Mishin, Y.: Atomistic modeling of capillary-driven grain boundary motion in Cu–Ta alloys. Acta Mater. **148**, 311–319 (2018)
28. Ma, K., Tao, H., Yang, H., Topping, T., Yousefiani, A., Lavernia, E.J., Schoenung, J.M.: Coupling of dislocations and precipitates: impact on the mechanical behavior of ultrafine grained Al–Zn–Mg alloys. Acta Mater. **103**(15), 153–164 (2016)
29. Jian, Z., Li, W., Zhao, B., Ren, F.: Direct measurement of the maximum pinning force during particle-grain boundary interaction via molecular dynamics simulations. Acta Mater. **148**, 1–8 (2018)
30. Dorin, T., Wood, K., Taylor, A., Hodgson, P., Stanford, N.: Effect of coiling treatment on microstructural development and precipitate strengthening of a strip cast steel. Acta Mater. **115**, 167–177 (2016)
31. Humphreys, F.J., Ardakani, M.G.: Grain boundary migration and Zener pinning in particle-containing copper crystals. Acta Mater. **44**(7), 2717–2727 (1996)
32. Smith, C.S.: Grains, phases, and interphases: an interpretation of microstructure. Metall. Technol. **175**, 15–51 (1948)
33. Kirklin, S., Saal, J.E., Hegde, V.I., Wolverton, C.: High-throughput computational search for strengthening precipitates in alloys. Acta Mater. **102**, 125–135 (2016)
34. Kad, B.K., Hazzledine, P.M.: Monte Carlo simulations of grain growth and Zener pinning. Mater. Sci. Eng. A **238**(1), 70–77 (1997)
35. Gladman, T.: On the theory of the effect of precipitate particles on grain growth in metals. Proc. R. Soc. Lond. **294**(1438), 298–309 (1966)
36. Nes, E., Ryum, N., Hunderi, O.: On the Zener drag. Acta Metall. **33**(1), 11–22 (1985)
37. Barnett, M.R., Wang, H., Guo, T.: An Orowan precipitate strengthening equation for mechanical twinning in Mg. Int. J. Plast. **112**, 108–122 (2019)
38. Tang, S., Xin, T., Xu, W., Miskovic, D., Sha, G., Quadir, Z., Ringer, S., Nomoto, K., Birbilis, N., Ferry, M.: Precipitation strengthening in an ultralight magnesium alloy. Nat. Commun. **10**(1), 1003 (2019)
39. He, J.Y., Wang, H., Huang, H.L., Xu, X.D., Chen, M.W., Wu, Y., Liu, X.J., Nieh, T.G., An, K., Lu, Z.P.: A precipitation-hardened high-entropy alloy with outstanding tensile properties. Acta Mater. **102**, 187–196 (2016)
40. Fang, Q.H., Liu, Y.W.: Size-dependent elastic interaction of a screw dislocation with a circular nano-inhomogeneity incorporating interface stress. Scr. Mater. **55**(1), 99–102 (2006)
41. Fang, Q.H., Li, L., Jia, L., Hongyu, W., Zaiwang, H., Bin, L., Yong, L., Liaw, P.K.: A statistical theory of probability-dependent precipitation strengthening in metals and alloys. J. Mech. Phys. Solids **122**, 177–189 (2019)
42. Koju, R.K., Darling, K.A., Kecskes, L.J., Mishin, Y.: Zener pinning of grain boundaries and structural stability of immiscible alloys. JOM **68**(6), 1596–1604 (2016)
43. Song, K., Aindow, M.: Grain growth and particle pinning in a model Ni-based superalloy. Mater. Sci. Eng. A **479**(1–2), 365–372 (2008)
44. Wörner, C.H., Hazzledine, P.M.: Grain growth stagnation by inclusions or pores. JOM **44**(9), 16–20 (1992)
45. Gutkin, M.Y., Kolesnikova, A.L., Ovid'Ko, I.A., Skiba, N.V.: Rotational deformation mechanism in fine-grained materials prepared by severe plastic deformation. J. Metastab. Nanocryst. Mater. **12**(12), 47–58 (2002)
46. Romanov, A.E., Vladimirov, V.I.: Disclinations in solids. Phys. Status Solidi **78**(1), 11–34 (2010)
47. Gutkin, M.Y., Kolesnikova, A.L., Ovidko, I.A., Skiba, N.V.: Rotational deformation mechanism in fine-grained materials prepared by severe plastic deformation. J. Metastab. **12**(12), 47–58 (2002)
48. Ringer, S.P., Li, W.B., Easterling, K.E.: On the interaction and pinning of grain boundaries by cubic shaped precipitate particles. Acta Metall. **37**(3), 831–841 (1989)
49. Schäfer, J., Albe, K.: Competing deformation mechanisms in nanocrystalline metals and alloys: coupled motion versus grain boundary sliding. Acta Mater. **60**(17), 6076–6085 (2012)
50. Caillard, D., Mompiou, F., Legros, M.: Grain-boundary shear-migration coupling. II. Geometrical model for general boundaries. Acta Mater. **57**(8), 2390–2402 (2009)
51. Mompiou, F., Legros, M., Caillard, D.: SMIG model: a new geometrical model to quantify grain boundary-based plasticity. Acta Mater. **58**(10), 3676–3689 (2010)
52. Chan, H.M., Humphreys, F.J.: Effect of particle stimulated nucleation on orientation of recrystallized grains. Metal Sci. J. **18**(11), 527–530 (2013)
53. Wusatowska-Sarnek, A.M., Miura, H., Sakai, T.: Nucleation and microtexture development under dynamic recrystallization of copper. Mater. Sci. Eng. A **323**(1), 177–186 (2002)
54. Robson, J.D., Henry, D.T., Davis, B.: Particle effects on recrystallization in magnesium-manganese alloys: particle-stimulated nucleation. Acta Mater. **57**(9), 2739–2747 (2009)
55. Pereloma, E.V., Mannan, P., Casillas, G., Saleh, A.A.: Particle stimulated nucleation during dynamic and metadynamic recrystallisation of Ni–30%Fe–Nb–C alloy. Mater. Charact. **125**, 94–98 (2017)
56. Saifei, Z., Zeng, W., Zhou, D., Lai, Y., Qinyang, Z.: The particle stimulated nucleation in Ti–35V–15Cr–0.3Si–0.1C alloy. Mater. Lett. **166**, 317–320 (2016)
57. Sakai, Taku, Belyakov, Andrey, Kaibyshev, Rustam, Miura, Hiromi, Jonas, John, J.: Dynamic and post-dynamic recrystallization under hot, cold and severe plastic deformation conditions. Prog. Mater. Sci. **60**(1), 130–207 (2014)
58. Chan, H.M., Humphreys, F.J.: The recrystallisation of aluminium-silicon alloys containing a bimodal particle distribution. Acta Metall. **32**(2), 235–243 (1984)
59. Devaraj, A., Wang, W., Vemuri, R., Kovarik, L., Jiang, X., Bowden, M., Trelewicz, J.R., Mathaudhu, S., Rohatgi, A.: Grain boundary segregation and intermetallic precipitation in coarsening resistant nanocrystalline aluminum alloys. Acta Mater. **165**, 698–708 (2019)

60. Shen, Y.F., Guan, R.G., Zhao, Z.Y., Misra, R.D.K.: Ultrafine-grained Al–0.2Sc–0.1Zr alloy: the mechanistic contribution of nano-sized precipitates on grain refinement during the novel process of accumulative continuous extrusion. Acta Mater. **100**, 247–255 (2015)
61. Wu, H., Wen, S.P., Huang, H., Li, B.L., Wu, X.L., Gao, K.Y., Wang, W., Nie, Z.R.: Effects of homogenization on precipitation of Al 3 (Er,Zr) particles and recrystallization behavior in a new type Al–Zn–Mg–Er–Zr alloy. Mater. Sci. Eng. A **689**(Complete), 313–322 (2017)

Publisher's Note Springer Nature remains neutral with regard to jurisdictional claims in published maps and institutional affiliations.